A Numerical Study of a Mesoscale Convective System during TOGA COARE. Part II: Organization

BADRINATH NAGARAJAN* AND M. K. YAU

Department of Atmospheric and Oceanic Sciences, McGill University, Montreal, Quebec, Canada

DA-LIN ZHANG

Department of Meteorology, University of Maryland, College Park, College Park, Maryland

(Manuscript received 17 April 2003, in final form 17 October 2003)

ABSTRACT

In Part I, the authors presented a successful numerical simulation of the life cycle of a warm-pool mesoscale convective system (MCS) that occurred on 15 December 1992 during the Tropical Ocean Global Atmosphere Coupled Ocean–Atmosphere Response Experiment. In this study, the simulation results of Part I are diagnosed to investigate the organization of the MCS and the convective onsets that occurred during the growing and mature stages of the MCS.

During the life cycle of the MCS, four convective onsets occur in the presence of large-scale ascent, convective available potential energy (CAPE), and surface potential temperature drop-off (SPTD). It is found that the first convective onset is caused by the existence of upward motion, CAPE, and SPTD in the model initial conditions. The second convective onset is regulated by the favorable occurrence of SPTD. The third and fourth convective onsets arise from the development of upward motion associated with the westward propagation of the quasi-2-day wave. The four mesoscale precipitation features clustered together to form the MCS in response to the evolution of the vertical motion field.

The organization of the MCS is characterized by the presence of a midtropospheric mesovortex situated near the position of the first convective onset. Analysis of the relative vorticity (RV) budget indicates that the mesovortex originates and intensifies largely from vortex stretching induced by deep convective heating. A decrease in RV above (below) the mesovortex arises because of the combined effects of the tilting and horizontal advection terms (the tilting, stretching, and solenoidal terms). Our results suggest that the mesovortex played little role in the subsequent onsets (i.e., second, third, and fourth) and that other warm-pool MCSs occurring near the transequatorial flow are likely to be associated with mesovortices.

1. Introduction

Warm-pool convection is organized on many scales. On the largest and smallest length scales are the supercloud clusters and individual convective cells. The intermediate scale is represented by mesoscale convective systems (MCSs). In turn, an MCS is composed of one or more mesoscale precipitation features (MPFs) that define its mesoscale organization (Tollerud and Esbensen 1985). Convection over the warm pool has been studied using satellite and radar data, but numerical studies are few in number.

Several studies of MPFs using infrared imagery highlighted the clustering behavior of warm-pool convection (e.g., Mapes and Houze 1993; Mapes 1993). Mapes (1993) suggested that the clustering of MPFs cannot be attributed solely to the large-scale flow because of the strong feedback between deep convection and the large-scale circulation. He showed that compensating vertical motions associated with deep convection renders the mesoscale vicinity favorable for the development of new convection and may be responsible for the clustering of MPFs. The work of Johnston (1981) was the first observational study of mesoscale convective vortices (MCVs) occurring in association with midlatitude mesoscale convective complexes (MCCs). Recently, Chong and Bousquet (1999) also reported a near-equatorial MCV associated with the 13 December 1992 Tropical Ocean Global Atmosphere Coupled Ocean–Atmosphere Response Experiment (TOGA COARE) MCS, indicating that MCVs may play an important role in the organization and development of convection (Zhang and Fritsch 1987; Bartels and Maddox 1991). Thus large-scale circulation, compensating vertical motions asso-

* Current affiliation: Abdus Salam International Centre for Theoretical Physics, Trieste, Italy.

Corresponding author address: Dr. Badrinath Nagarajan, Abdus Salam International Centre for Theoretical Physics, PWC section, Strada Costiera 11, Trieste I-34014, Italy.
E-mail: badrinath.nagarajan@elf.mcgill.ca

ciated with deep convection, and the MCV-associated circulation are possible mechanisms that organize warm-pool convection.

On the other hand, MPFs appear as entities in radar reflectivity, and they are composed of convective and stratiform precipitation regions during the mature and dissipation stages (Leary and Houze 1979). Rickenbach and Rutledge (1998), using radar measurements, studied the organization of the MPFs in terms of the spatial distribution of precipitation. They concluded that over the 4-month TOGA COARE intensive observing period (IOP), about 50% of deep convection exhibited linear organization at length scales of about 100 km. LeMone et al. (1998) investigated the relation between the orientation of warm-pool deep convection and the vertical wind shear at the middle and low levels. They found that a strong environmental vertical wind shear at low (mid) levels was associated with a shear-perpendicular (shear parallel) convective band. When both the mid- and low-level shears were strong, the structure of the MPF can be complex, depending on the direction of the midlevel shear with respect to the low-level shear. Specifically, when the midlevel shear was directed opposite to the low-level shear, secondary convective lines parallel to the midlevel shear extended rearward from the primary convective lines. However, when the midlevel shear was perpendicular to the low-level shear, only convective lines perpendicular to the low-level shear were present. Kingsmill and Houze (1999) analyzed 33 TOGA COARE precipitation systems over the 4-month period and concluded that the structure and time evolution of the COARE MPFs were in qualitative agreement with the conceptual model of convection proposed for the Global Atmospheric Research Program (GARP) Atlantic Tropical Experiment (GATE) by Leary and Houze (1979).

In Part I (Nagarajan et al. 2001, hereafter NYZ01), we presented a successful 16-h simulation of the life cycle of a class 4 (Yuter et al. 1995) MCS, initialized at 0400 UTC 15 December 1992, using an improved version of the Mesoscale Compressible Community (MC2) model (Benoit et al. 1997). The model included the solar and infrared radiation schemes (Garand and Mailhot 1990), the atmospheric boundary layer (ABL) processes of Benoit et al. (1989), the Kain–Fritsch (KF) cumulus parameterization (Kain and Fritsch 1990), the Betts–Miller shallow convection (Betts 1986), and the explicit microphysical processes (Kong and Yau 1997). In order to successfully simulate the MCS, NYZ01 introduced improvements to the model physical processes and the initial moisture field. The improvements to the physical processes included better convective initiation and the detrainment of cloud water, rainwater, and ice particles in the KF convective scheme, as well as the modifications suggested by Fairall et al. (1996) to compute surface fluxes for weak surface flows over the warm pool. The convective gust effects on the surface fluxes are also incorporated following Jabouille et al. (1996). Interested readers are referred to NYZ01 for further details.

The time evolution of an MPF comprises the initiation, developing, and dissipating stages (Leary and Houze 1979). In NYZ01, it was shown that with the improved initial conditions and model physics, the model reproduced realistically the evolution of the anvil cloud fraction, the four convective onsets, and the large-scale flow features. Note that a convective onset is defined as the initiation of one or more MPFs. It was also shown that the surface potential temperature drop-off (SPTD) was largely responsible for the successful prediction of the life cycle of the MCS. Three convective onsets associated with three simulated MPFs were initiated at 0600, 1100, and 1400 UTC (see Fig. 1). The last MPF was responsible for the merger of two entities S_1 and S_2, identified in the Geostationary Meteorological Satellite (GMS) infrared imagery at 0530 UTC. We also showed a fourth convective onset at the *mature stage* of the MCS (1700–2000 UTC). This onset is composed of two MPFs characterized by two NE–SW-oriented convective lines (L_1 and L_2) with stratiform precipitation located to their northwest (Fig. 1). Protat and Lemaitre (2001b) studied the structure of these MPFs during the period 1700–2045 UTC, making use of the airflow and spatial distribution of reflectivity derived from airborne Doppler radar measurements. They found that the MPFs shared several features typical of tropical squall lines. These include 1) leading convective line with trailing stratiform regions, 2) the generation of the stratiform clouds by evacuation of ice by a front-to-rear updraft, 3) an elevated vertical velocity maximum, 4) an upward transport of horizontal momentum by the convective and mesoscale updrafts, and 5) leading convection oriented perpendicular to the low-level vertical wind shear. However, they also noted that in some aspects, there are significant departures of the MPF structures from the classical tropical squall lines, with a strong forward and rearward splitting updraft located above an altitude of 10 km [see Fig. 7 of Protat and Lemaitre (2001b) for a conceptual model].

One of the objectives of TOGA COARE is to understand the processes leading to the organization of warm-pool convection (Webster and Lukas 1992). Life cycle studies of warm-pool MCSs are rare, as observational studies generally focus only on the mature and dissipation stages. To fill this gap, we undertook an analysis of the control (CTL) simulation of NYZ01 to investigate the processes responsible for the four convective onsets and the organization of the 15 December 1992 TOGA COARE MCS. Since Chong and Bousquet (1999) is the first observational study to point out several features common to both a near-equatorial MCV and MCVs occurring in midlatitude MCSs, we shall analyze our case to determine if an MCV occurs and how it may develop.

This paper is organized as follows. The next section contains a study of the physical processes leading to the

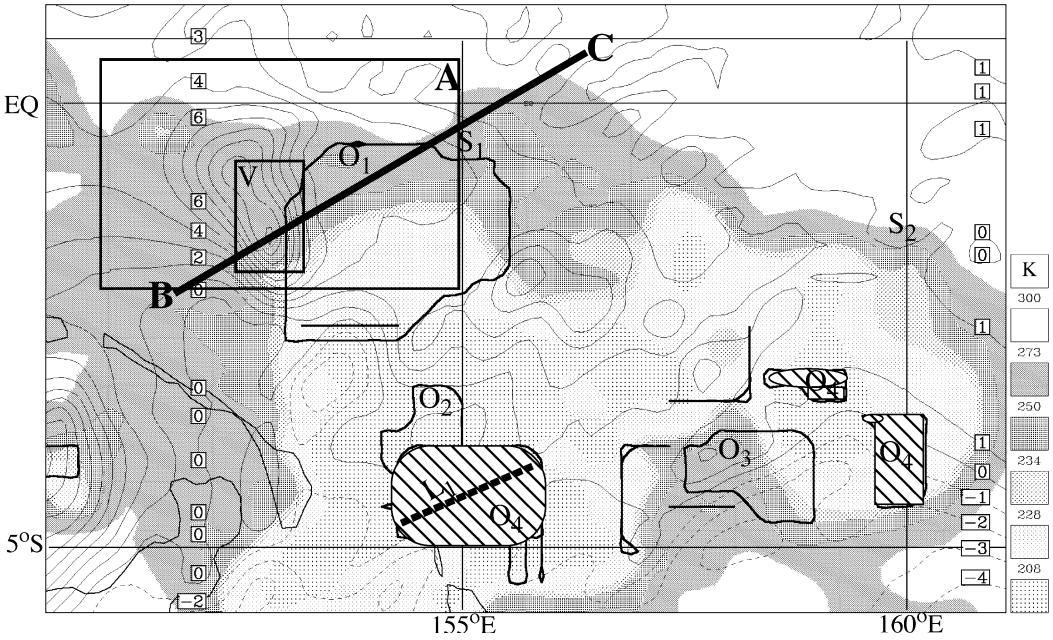

FIG. 1. The 15 Dec 1992 MCS. The shaded area depicts brightness temperatures (K) at 1630 UTC from the Japanese GMS. The 0600, 1100, and 1400 UTC convective onsets, denoted by O_1, O_2, and O_3, respectively, are enclosed by thick solid lines. The convective onset occurring at 1700 UTC (O_4), accompanied by a simulated convective line L_1 (thick dashed), is shown by the stippled areas. The symbols S_1 and S_2 represent the location of the two entities at 0530 UTC (refer to NYZ01 for details). The thin contour lines indicate the 500-hPa relative vorticity at 1600 UTC in units of 10^{-5} s^{-1}. A mesoscale convective vortex is located in box V, which is used for the computation of the relative vorticity budget. Box A is used to compute the time evolution of the areal average of relative vorticity and horizontal divergence. The line BC denotes the location of the vertical cross section shown in Fig. 15.

four convective onsets. Section 3 presents observational evidence, the development of a warm-core MCV, and its kinematic description. It also describes a relative vorticity budget analysis of the MCV. A summary and conclusions are given in the final section.

2. Convective onsets

LeMone et al. (1998) suggested two possible organizing mechanisms for warm-pool convection. These are large-scale flow (e.g., the ITCZ) and self-organization in the absence of large-scale forcing. One such self-organizing mechanism was proposed by Mapes (1993), who suggested that clustering behavior of the warm-pool convection arises because of lower-tropospheric ascent induced by gravity waves associated with the compensational subsidence in the region heated by an MCS. In a recent study of synoptic-scale processes associated with this particular MCS, Protat and Lemaitre (2001a) concluded that two factors governed the initiation and evolution of the MCS: convective available potential energy (CAPE) and low-level convergence (below 850 hPa). Thus, warm-pool convection is favored by the presence of large-scale ascent and CAPE.

Chen and Houze (1997) suggested that warm-pool convection is regulated by ABL processes. That is, the onset of the late afternoon MCSs over the warm pool is due to the diurnal warming of the atmospheric surface layer. Raymond (1995) proposed that deep convection over the warm pool is associated with a near-zero convective deficit (defined as the difference between the saturation equivalent potential temperature of the cloud layer and the boundary layer equivalent potential temperature). Crook (1996) is of the view that convective initiation over land in warm and moist environments is sensitive to SPTD. NYZ01 extended the use of SPTD to the initiation of oceanic warm-pool convection by defining the SPTD as $\theta_{SST} - \overline{\theta}_{ABL}$, where θ_{SST} and $\overline{\theta}_{ABL}$ are the sea surface potential temperature and the averaged ABL potential temperature, respectively. When there is a large reduction in convective inhibition (CIN) for a large SPTD, convective initiation becomes highly probable. NYZ01 demonstrated that for a threshold value of SPTD, the overlap between the observed area of convective onset and the area enclosed by the SPTD contour is maximized. Hence, a necessary condition for a convective onset in the simulation is that the SPTD exceeds the threshold value. Thus we address below four convective onsets, as mentioned in the preceding section, in terms of SPTD, large-scale ascent, and CAPE.

a. Convective onset at 0600 UTC

Figure 2a shows the 900-hPa vertical motion at 0400 UTC and the areas with SPTD > 1.25°C (shaded). The first onset occurs in a region of ascending motion as-

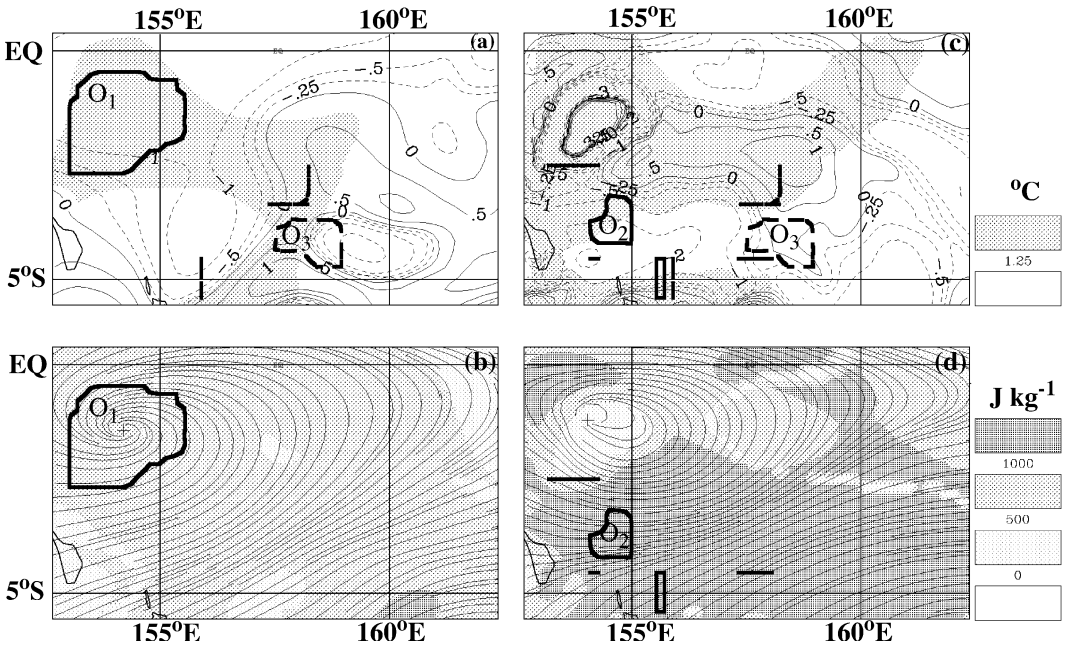

FIG. 2. (top) The 900-hPa vertical motion (10^{-1} Pa s^{-1}) and SPTD (shaded) exceeding 1.25°C at (a) 0400 and (c) 0800 UTC, and (bottom) the 900-hPa streamlines and CAPE (shaded) in units of J kg^{-1} at (b) 0400 and (d) 0800 UTC. The CAPE is computed using the mean temperature and specific humidity of the lowest 60-hPa air layer. The 0600, 1100, and 1400 UTC convective onsets are indicated by symbols O_1, O_2, and O_3, respectively. The contours for vertical motion shown are −3.0, −2.0, −1.0, −0.5, −0.25, 0.0, 0.5, 1.0, 2.0, 3.0 in units of 10^{-1} Pa s^{-1}.

sociated with the transequatorial (TE) flow (Ramage 1971), with moderate values of CAPE (shaded areas in Fig. 2b) and the SPTD criterion satisfied (>1.25°C). The CAPE is computed using the mean temperature and specific humidity of the lowest 60-hPa air layer (typically between 1000 and 940 hPa). Thus, the onset is characterized by the existence of large-scale ascent, CAPE, and favorable SPTD in the model initial conditions (0400 UTC).

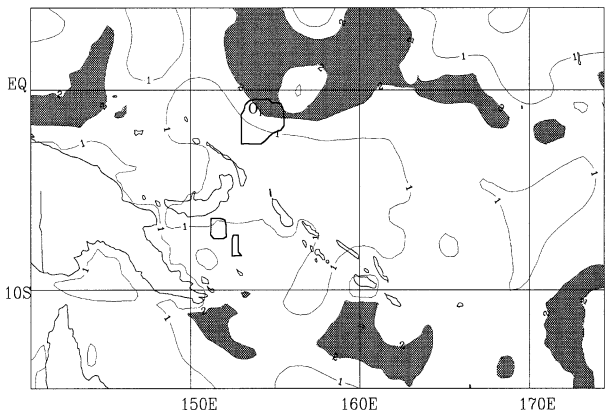

FIG. 3. Estimated diurnal amplitude of the SST for 15 Dec 1992 over the model domain. Areas of ≥2.0°C are shaded. The area of the 0600 UTC 15 Dec 1992 convective onset is depicted by a thick solid line.

b. Convective onset at 1100 UTC

Figure 2c shows the 900-hPa vertical motion and areas with SPTD > 1.25°C (shaded) at 0800 UTC. The onset occurs in the confluence zone of westerlies and southwesterlies, which is located south of the center of the TE flow (Fig. 2d). The onset area is also characterized by moderate CAPE. Even though Figs. 2a and 2b reveal the existence of ascending motion and moderate CAPE at 0400 UTC, a favorable SPTD does not exist at this time. However, the SPTD becomes favorable over much of the area of the onset between 0400 and 0800 UTC (Figs. 2a,c). Thus, the timing of the onset is regulated by the favorable occurrence of SPTD between 0400 and 0800 UTC.

Recall that we defined SPTD = $\theta_{SST} - \overline{\theta}_{ABL}$ with the model simulation using a temporally fixed SST. However, significant diurnal change in SST occurs over the warm pool (Webster et al. 1996), which depends on daily average surface wind speed, precipitation rate, and the peak surface solar insolation (Webster et al. 1996). Figure 3 shows the estimated diurnal amplitude of SST for 15 December 1992 using the regression relation suggested by Webster et al. (1996). Areas between 0°–5°N, 150°–165°E exhibit higher SST amplitudes. This arises because of clear skies (or higher surface insolation) combined with weak surface wind speeds. The region 0°–5°S, 155°–160°E displays SST amplitudes less than 1°C primarily because of high wind speeds (>4 m s^{-1};

TABLE 1. The pre-onset period (times in parentheses in column 1) potential temperature budget averaged over the depth of the atmospheric boundary layer and the convective onset region (times for convective onsets shown left of pre-onset times in column 1) in °C day^{-1}. Columns 2–10 show respectively the local heating rate, the heating rates due to horizontal advection, vertical advection, longwave cooling (LC), vertical diffusion (VD), deep convection (DC), shallow convection (SC), explicit microphysics (EM), and horizontal diffusion (HD). The solar heating rate is small because of evening conditions and is not shown.

Onset (UTC)	$\frac{\partial\theta}{\partial t}$	$-\boldsymbol{v}\cdot\nabla\theta$	$-w\frac{\partial\theta}{\partial z}$	LC	VD	DC	SC	EM	HD
1100 (0800)	−1.97	−0.46	−0.9	−2.6	1.1	-5.0×10^{-5}	6.2×10^{-3}	0.8	0.19
1400 (1200)	−3.78	−0.85	−1.9	−2.51	1.78	-1.32×10^{-4}	-2.16×10^{-4}	-7.78×10^{-2}	−0.2

not shown). Thus the region (0°–5°S, 155°–160°E) of the four convective onsets (Fig. 1) exhibits SST amplitudes less than 1°C. The peak SST over the warm pool occurs between 1200 and 1400 LST (=UTC + 10 h at 150°E; Chen and Houze 1997). The 1100, 1400, and 1700 UTC convective onsets occur during the nighttime when the temporal variation in SST is small, and since the diurnal variation in SST is confined to the northern fringe of the 0600 UTC onset (Fig. 4), we do not expect any significant impact on the timing of the onsets.

With little variation of the surface pressure with time and a temporally fixed SST in the simulation, the increase in SPTD is caused by a decrease in the ABL potential temperature. Table 1 shows the magnitudes of the various terms in the potential temperature equation averaged over the ABL and the onset region at 0800 UTC. The ABL depth is obtained from the model simulation. The ABL potential temperature budget shows that the decrease in potential temperature arises mainly from the processes of longwave cooling (LC) and vertical and horizontal cold advection of potential temperature. This decrease is offset by the upward turbulent transfer of sensible heat (VD) in the ABL and cloud condensation (EM) near the ABL top. This suggests that the vertical cold advection of θ associated with the large-scale ascent in the confluence zone (Fig. 2d) and the longwave cooling are mainly responsible for the SPTD increase, which in turn triggers the 1100 UTC convective onset.

c. Convective onset at 1400 UTC

At 0400 UTC, Fig. 2a shows an area of favorable SPTD and upward motion in the region of the third convective onset. However, by 0800 UTC the SPTD becomes unfavorable (i.e., SPTD $<$ 1.25°C), and the region is characterized by weak downward motion (Fig. 2c). The existence of downward motion and the absence of a favorable SPTD precludes the onset of convection between 0400 and 0800 UTC.

By 1200 UTC, the 900-hPa vertical motion becomes upward in the region of the third convective onset (see Fig. 4a). The ABL budget at 1200 UTC shows that the vertical and horizontal cold advection of potential temperature, along with the LC, account for the cooling of the ABL (Table 1). The fact that upward motion developed between 0800 and 1200 UTC and that it contributes significantly (−1.9° day^{-1}) to the cooling of the ABL suggests that the large-scale vertical motion, in addition to providing a deep tropospheric ascent favorable for the outbreak of convection, also renders the SPTD favorable. Despite the existence of CAPE in the region of the onset between 0400 and 1200 UTC, it is the development of upward motion that regulates the convective onset. We therefore turn our attention to the factors that cause the change in vertical motion at and after 1100 UTC.

Mapes (1993) suggested a possible mechanism for the development of ascending motion at the low levels in the region of convective onset. He specified a heating profile similar to that of a tropical MCS and showed that upward displacement occurs in the lowest 4 km in the vicinity of the heat source as a result of gravity waves set off by compensational subsidence associated with deep convection. In order to study the role of Mapes' gravity wave mechanism in the development of low-level upward motion we performed a DRY run in which all condensational heating associated with deep convection and the explicit microphysical processes were turned off. Since deep convection is absent in the DRY run, the mechanism for the launching of gravity waves proposed by Mapes is eliminated. Therefore, the upward motion in the region of convective onset should be absent if the Mapes mechanism is operative.

The vertical velocities at 900 hPa from the CTL simulation and the DRY experiment valid at 0800 and 1200 UTC are shown in Figs. 5a–d. At 0800 UTC, the region of the convective onset is marked by subsidence in the CTL run, but there are weak ascending and descending motions occurring in the DRY run (Figs. 5a,b). At 1200 UTC, the DRY and CTL runs indicated ascending motion in the onset region (Figs. 5c,d), suggesting that another process may be responsible for the development of ascending motions at 1200 UTC.

Figure 6a depicts the vertical cross section of the departure of the zonal winds from the mean values at each level at 0400 UTC from the DRY experiment. The positive midtropospheric wind anomaly between 140.6° and 149.0°E is compensated by negative anomalies near the surface and at the tropopause levels. Although Mapes (1993) suggested that such wind anomaly structures is accompanied by ascending (descending) motion below (above) 600 hPa (see his Fig. 3), our results indi-

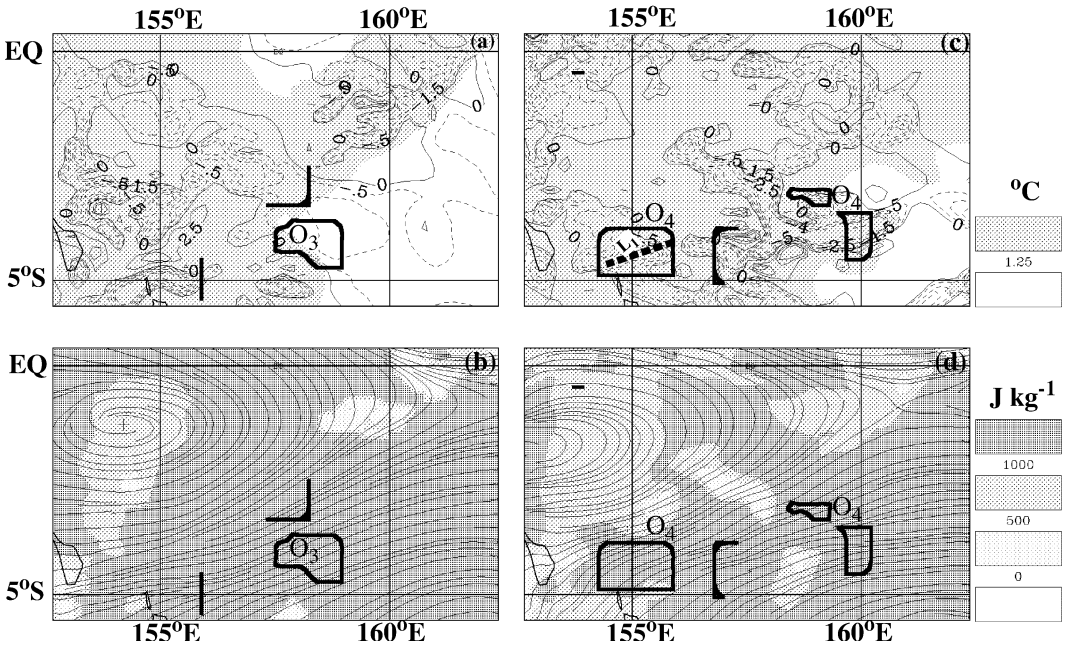

FIG. 4. As in Fig. 2 but for (a), (b) 1200 and (c), (d) 1700 UTC. The 1400 and 1700 UTC convective onsets are indicated by symbols O_3 and O_4, respectively. The thick dashed line in (c) shows the orientation of the convective line L_1 associated with the 1700 UTC convective onset. The relation of L_1 to the rest of the MCS can be seen in Fig. 1. The vertical motion contours shown are -10.0, -5.0, -4.0, -2.5, -1.5, -0.5, 0.0, 2.5, 3.5, 4.5, 10.0 in units of 10^{-1} Pa s^{-1}.

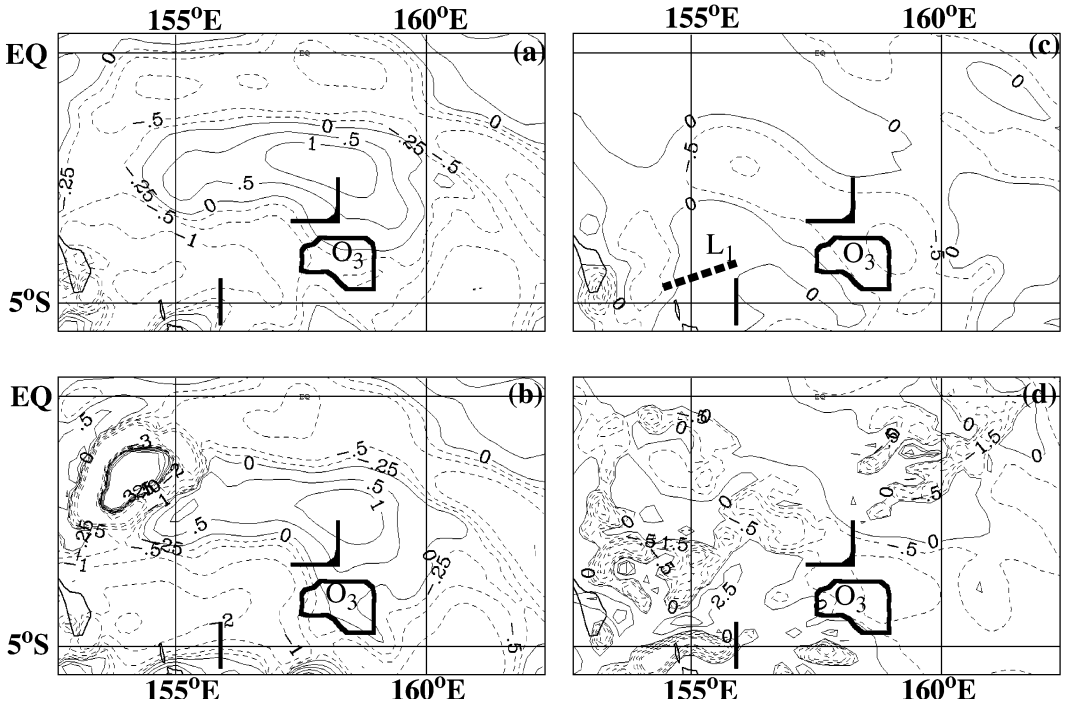

FIG. 5. The 900-hPa vertical motion for the (top) DRY simulation at (a) 0800 and (c) 1200 UTC and for the (bottom) CTL simulation at (b) 0800 and (d) 1200 UTC 15 Dec 1992. Dashed (solid) lines represent ascending (descending) motion in units of 10^{-1} Pa s^{-1}. The third convective onset is indicated by the symbol O_3. The thick dashed line in (c) denotes the convective line L_1 that occurred during the mature stage of the MCS.

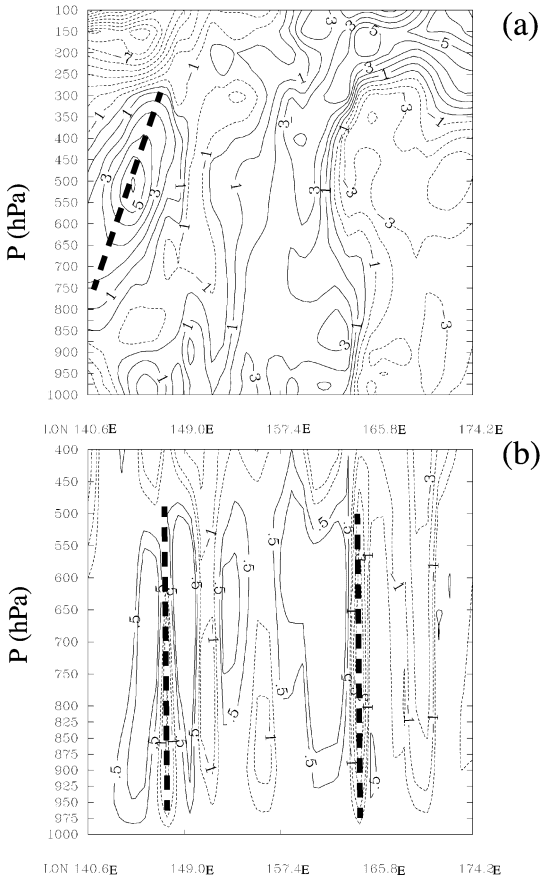

FIG. 6. Vertical cross section of (a) the zonal wind (m s^{-1}), with the mean at each level subtracted out, and (b) the vertical motion (10^{-1} Pa s^{-1}) from the DRY simulation valid at 0400 UTC 15 Dec 1992. The section is taken along 2.8°S latitude from 140.6°–174.3°E. The contour interval for the zonal wind is 1 m s^{-1}. Vertical motion contours are −7.0, −5.0, −3.0, −2.0, −1.0, −0.5, 0.5, 1.0, 3.0 Pa s^{-1}. The thick dashed lines indicate the vertical structure associated with a quasi-2-day wave.

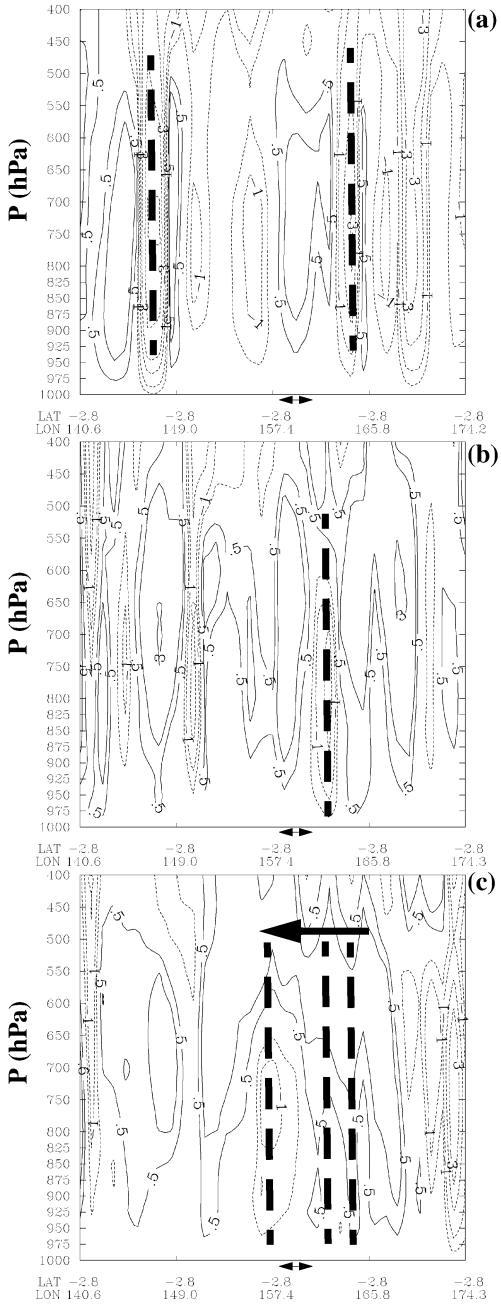

FIG. 7. Longitude–height section of vertical motion (10^{-1} Pa s^{-1}) taken along 2.8°S latitude from the DRY run valid at (a) 0400, (b) 0800, and (c) 1200 UTC 15 Dec 1992. The thick dashed lines indicate the vertical structure associated with a quasi-2-day wave. The vertical structures associated with the quasi-2-day wave at 0400 and 0800 UTC are also indicated in (c). The direction of propagation of the wave is indicated by the thick solid arrow in (c). The region of convective onset around 157.1°E is marked by a double arrow.

cated no such vertical motion in the present case (Fig. 6b). The 140.6° and 149.0°E longitudinal band is also quite a distance from the region of the 1400 UTC convective onset. On the other hand, over the region of the convective onsets at 0800 and 1200 UTC (Figs. 7b,c), the structure of the vertical motion is similar to that associated with the Mapes mechanism, but the zonal wind anomaly bears no such resemblance. Even if we were to assume that the Mapes mechanism was responsible for these wind and vertical motion structures, its propagation speed would have to be about 23° day^{-1} [obtained by using a buoyancy period of 10 min and a vertical wavelength of 16 km as the height of the tropopause in Eq. (2) of Mapes (1993)], quite different from a propagation speed of 12°–15° day^{-1} determined from our simulation. Thus it is our contention that, although the structures of zonal wind anomaly and vertical motion may suggest an association with the Mapes mechanism, the discrepancy in the propagation speeds points to another process that is responsible for the development of ascending motion at 1200 UTC.

Several studies have revealed a close connection between tropical convection and the large-scale atmospheric waves. Numaguti (1995) reported the near ab-

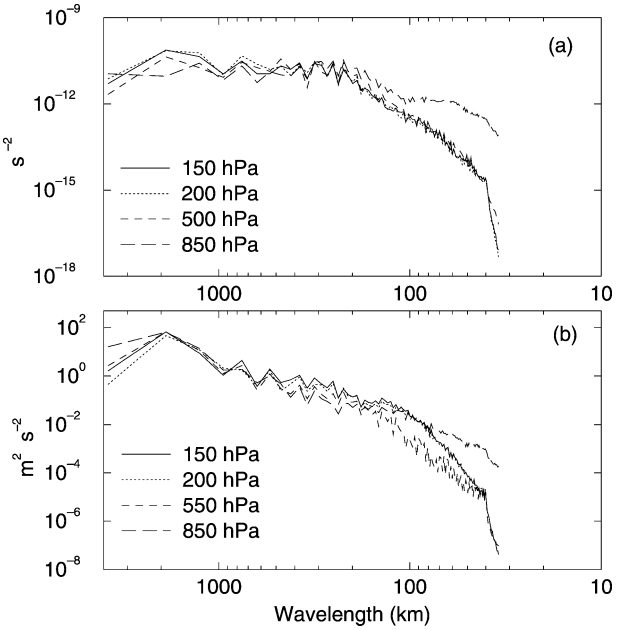

FIG. 8. Wavenumber spectra of the (a) horizontal divergence and (b) zonal wind component as a function of the horizontal wavelength (km) from the DRY run at 1400 UTC 15 Dec 1992. The spectra are shown at 150-, 200-, 550-, and 850-hPa pressure levels.

sence of the 4–6- and 15–20-day wave activity in the region of S_1 and S_2 (Fig. 1). Even if these waves were present, their horizontal length scales are too large to explain the mesoscale ascent seen in the region of onset. Takayabu et al. (1996) and Chen and Houze (1996), however, suggested that a quasi-2-day wave can be associated with warm-pool convection. Chen and Houze (1996) noted the existence of three well-defined westward propagating 2-day waves between 140° and 165°E in the vicinity of a latitudinal band (1°N–10°S) for the period of 11–15 December. From a time series of the horizontal distribution of blackbody temperature data, Takayabu et al. (1996) reported the existence of eight quasi-2-day wave events from 10 to 16 and 21 to 27 December 1992 (their Fig. 4). Specifically, there appears to be an event between 14 and 16 December, suggesting the presence of the wave during the occurrence of the 15 December 1992 MCS.

Since our simulation is only 16 h long, we present evidence for the existence of a quasi-2-day wave by computing the spectra of horizontal divergence and zonal wind using the technique of Errico (1985). The quasi-2-day wave exhibits a wavelength of 2000–2500 km (Takayabu et al. 1996). Figure 8 shows the 1400 UTC spectra of horizontal divergence and zonal wind component from the DRY run. There exists a peak at 1900 km in the zonal wind (Fig. 8b) and divergence spectra (Fig. 8a), suggesting the presence of a quasi-2-day wave.

Takayabu et al. (1996) identified the quasi-2-day wave from power spectrum analysis of satellite data and linked it to the westward propagating $n = 0$ and $n = 1$ inertia–gravity waves. The wave possesses a phase speed of 12°–15° day^{-1}. The amplitude of the wave indicates a maximum at 3°S, while the zonal wind components exhibit peak values at 850, 550, and 175 hPa. Vertically, the wind components show an eastward tilt with height. The source of the wave is found to be located around 175 hPa. The composite vertical structures of the zonal, meridional wind components, and the horizontal divergence were related to various stages of the life cycle of an MCS.

It is evident that the zonal wind axis tilts eastward with height around 2.8°S, 140.6°E (Fig. 6a). A less conspicuous eastward tilt can also be found around 2.8°S, 157.4°E. Note that the amplitudes peak at 550 and 175 hPa with magnitudes of 6 m s^{-1}, in good agreement with the values reported in Takayabu et al. (1996). Corresponding to the two vertical structures in the zonal winds are two regions with strong upward motion indicated by thick dashed lines (Fig. 6b). The horizontal separation between these two features is around 2000 km and is in agreement with the wavelength of about 2000–2500 km attributed to the 2-day wave. Thus, the vertical structure and horizontal wavelength associated with the zonal and vertical motion are consistent with the presence of a quasi-2-day wave as reported by Takayabu et al. (1996). It may be mentioned that, although in the DRY experiment all latent heating due to deep convection and explicit microphysics is turned off, the initial conditions are the same as that of the CTL experiment and hence contain the vertical motion field associated with the MCSs present at the model initial time (0400 UTC).

To determine the propagation speed of the wave and its role in triggering the convective onset, we plotted in Fig. 7 the vertical motion at 0400, 0800, and 1200 UTC along the 2.8°S latitude. At 0400 UTC (Fig. 7a) there is subsidence over the onset region. Although the vertical motion structure moves westward between 0400 and 0800 UTC because of the westward propagation of the quasi-2-day wave, the onset region still experiences downward motion precluding the onset of deep convection (Fig. 7b). However by 1200 UTC, the onset region exhibits upward motions with further westward propagation of the wave (Fig. 7c). Clearly, the convective onset is modulated by the propagation of the quasi-2-day wave. The westward propagation speed inferred from Fig. 7c is consistent with a propagation speed of 12°–15° day^{-1} reported by Takayabu et al. (1996). Therefore, we conclude that a 2-day wave is present in the region of convective onset, and it regulates the mesoscale vertical motion field to trigger the convective onset at 1400 UTC.

Our simulation results suggest that the mechanism for lifting at low levels, proposed by Mapes (1993), is not responsible for convective onset. In addition, the merger of S_1 and S_2 (Fig. 1) is associated with the outbreak of new convection triggered by the buildup of ascending motion caused by the westward propagation of the qua-

si-2-day wave. The ascending motion lowers the ABL potential temperature and results in a favorable SPTD while providing a deep tropospheric ascent favorable for the onset.

d. Convective onset at 1700 UTC

This onset occurred during the mature stage of the MCS and was responsible for the convective line L_1 associated with an MPF (Fig. 1). In the area of this onset, CAPE existed between 0400 and 1700 UTC (Figs. 2b,d and 4b,d). Also, the SPTD was favorable from 1200 UTC onward (Fig. 4a). However, a vertical cross section of the hourly vertical motion field from the CTL simulation taken along L_1 exhibited downward motion between 1200 and 1500 UTC but became upward at about 1600 UTC (not shown). This onset was therefore regulated by the occurrence of upward motion at 1600 UTC, given the favorable CAPE and SPTD at 1200 UTC.

Similar to the CTL simulation, the 900-hPa vertical motion field along L_1 in the DRY simulation at 1200 UTC is largely downward but of weaker amplitude (Figs. 5c and 4a). Thus part of the downward motion over the onset region arises because of compensating subsidence associated with deep convection lying north and south of L_1 (Fig. 4a) and the evolution of the large-scale vertical velocity field. A latitudinal vertical cross section of the zonal winds between 0400 and 1200 UTC (similar to Fig. 6 but taken along 4.2°S) confirms the existence of the 2-day wave (not shown). This suggests that the evolution of the vertical motion field over this onset region is also associated with the 2-day wave.

Recall from Fig. 6b that there were two vertical velocity structures associated with the 2-day wave along 2.8°S. Figure 9 shows a similar structure in the vertical velocity field near 157.4°E but along 4.2°S. The maximum 850-hPa vertical velocity, situated between 158.5° and 160.2°E at 1200 UTC propagates westward between 1200 and 1700 UTC (Figs. 9a–c). Thus, the large-scale descent evident at 1200 UTC in the vicinity of the onset (around 155°E) is associated with the 2-day wave. The westward propagation of the wave renders the motion upward by 1700 UTC (Fig. 9c). Therefore the onset of the convective line L_1 is regulated by the evolution of the vertical motion field that is controlled by the westward propagation of the 2-day wave as well as the compensating subsidence associated with convection lying to the north and south of L_1.

The 15 December 1992 MCS develops because of four convective onsets (associated with different MPFs; Fig. 1), with the individual MPFs being initiated independent of one another. The mesoscale vertical motion largely controls their initiation and is associated with the existence of a TE circulation and the westward propagation of a quasi-2-day wave. The gravity wave mechanism suggested by Mapes (1993) does not play a role in the initiation of the onsets. Thus, the formation of the MCS may be viewed as arising from the clustering of the MPFs initiated at 0600, 1100, 1400, and 1700 UTC where the evolution of the vertical motion field rather than the gravity wave mechanism is responsible for the clustering. Further, the existence of the 2-day wave and the TE circulation in the near-equatorial lat-

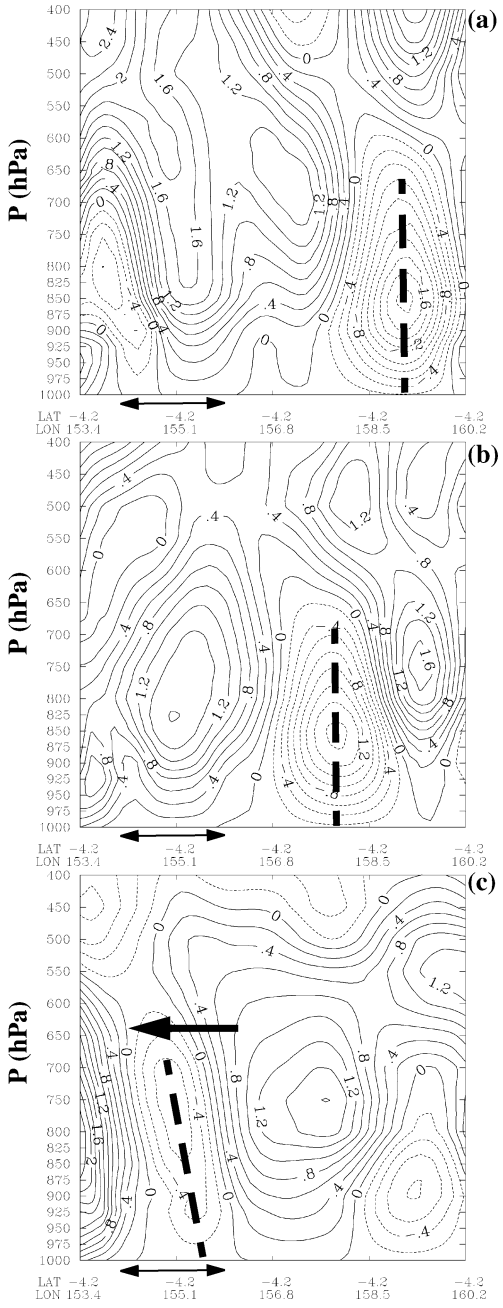

FIG. 9. Longitude–height section of vertical motion (10^{-1} Pa s^{-1}) taken along 4.2°S latitude from the DRY run valid at (a) 1200, (b) 1400, and (c) 1700 UTC 15 Dec 1992. The thick dashed lines indicate the vertical structure of the vertical motion associated with a quasi-2-day wave (near 157.4°E in Fig. 6). The direction of propagation of the wave is indicated by the thick solid arrow in (c). The region of convective onset around 155.0°E is indicated by the double arrow.

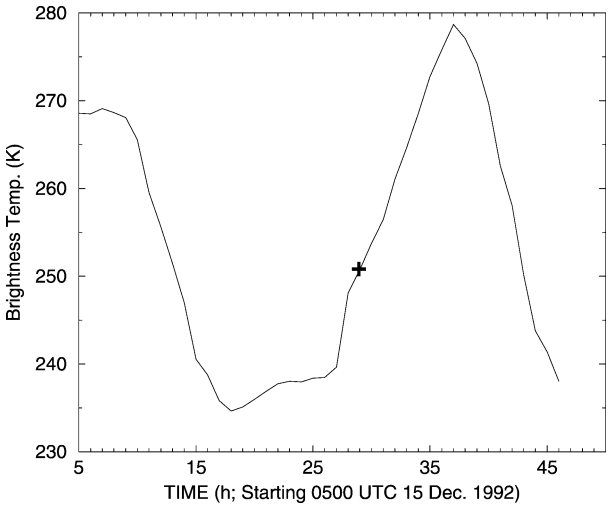

FIG. 10. The time evolution of the domain-averaged brightness temperature (K) from hourly GMS infrared satellite data. The average is performed over 0°–5°S and 150°–155°E. The "+" indicates the time of the *NOAA-11* AVHRR visible and infrared satellite imageries shown in Fig. 11.

itudes also may suggest an enhanced predictability of the MCS.

3. Mesoscale convective vortex

a. Development of an MCV

During the mature and dissipating stages of an MPF, a large area of stratiform precipitation generally occurs. The stratiform precipitation is frequently associated with mesovortices in the lower and middle troposphere. The MCV occurring in association with the midlatitude MCSs have been investigated using satellite data. Bartels and Maddox (1991) analyzed visible satellite data and showed that 50% of the MCVs were associated with MCCs. Johnston (1981) showed that most MCVs originate from short-lived and smaller-sized MCSs. Since an MCV is situated in the lower and middle troposphere, they are identified in the visible satellite imagery following the dissipation of the anvil cloud (Bartels and Maddox 1991). The visible data show rotating cloud patterns and are used to detect the presence of an MCV. Johnston (1981) used infrared data to infer the elevation above sea level of the MCV. Recently, Chong and Bousquet (1999) studied the 13 December 1992 TOGA COARE MCS and documented the occurrence of an MCV. The MCV region was characterized by a notch region in the infrared satellite imagery and the radar reflectivity field (their Figs. 1 and 4). The notch region was characterized by relatively warmer cloud-top temperature and lower radar reflectivity. We use the satellite data to provide qualitative evidence for the existence of an MCV in the 15 December 1992 TOGA COARE MCS.

Figure 10 shows the time evolution of the domain-averaged brightness temperature between 0530 UTC 15 December and 2330 UTC 16 December 1992. The domain (0°–5°S, 150°–155°E) over which the average is performed includes the 0600, 1100, and some portion of the 1700 UTC convective onsets (Fig. 1). It is evident from Fig. 10 that the cloud tops rapidly build up over the domain between 0530 and 1730 UTC, marking the growing stage of the MCS (NYZ01). This is followed by a small rise of brightness temperature (or reduced cloud-top heights) between 1730 UTC 15 December and 0330 UTC 16 December when the MCS attains its mature stage (NYZ01). Between 0330 and 1100 UTC 16 December the brightness temperature rises rapidly, signaling the dissipation of the anvil cloud associated with the MCS. The cloud-type change is consistent with the results of Miller and Fritsch (1991) for warm-pool convection. Since the anvil cloud at this time has dissipated, the midlevel circulations associated with the MCV should be apparent in the Advanced Very High Resolution Radiometer (AVHRR) visible data (Bartels and Maddox 1991). A rotating cloud pattern with an approximate size of 150 km is apparent in the visible data (Fig. 11). The cloud pattern is associated with brightness temperatures between 260 and 273 K (Fig. 11), which over the warm pool occurs between 450 and 600 hPa.

Figure 12 shows the 500-hPa simulated relative vorticity at 1600 UTC superposed with the 1130 UTC brightness temperature. A notch region appears in the vicinity of the simulated MCV. The notch cloud pattern is first evident at 0830 UTC (not shown). As in Chong and Bousquet (1999), the notch region is characterized by warm clouds (brightness temperature between 250 and 273 K). Thus the satellite data suggests the occurrence of an MCV in the midtroposphere with a diameter of 150 km.

Zhang and Fritsch (1987) reported the first numerical study of an MCV associated with a midlatitude mesoscale convective complex. Zhang (1992), on the basis of a numerical simulation of a midlatitude MCC, defined an MCV as a "significant concentration of positive relative vorticity of magnitude at least that of the local Coriolis parameter, eventually leading to the formation of a closed circulation." Recently, Chong and Bousquet (1999) documented an MCV over the warm pool that fits this definition very closely. We will present evidence for a simulated MCV in the region of the first convective onset following this definition.

We have indicated in Fig. 1a the 500-hPa relative vorticity maximum in box A relative to the three convective onsets and the entities S_1 and S_2. To examine the evolution of this vorticity maximum, we display in Fig. 13 the area-averaged relative vorticity and horizontal divergence as a function of pressure and time. Note the two maxima in the relative vorticity field: one centered around 850 hPa and the other around 550 hPa. Previous studies of MCSs generally indicate a single vorticity maximum, for example, occurring between 900 and 750 hPa in Zhang (1992) and near 500 hPa in Chong

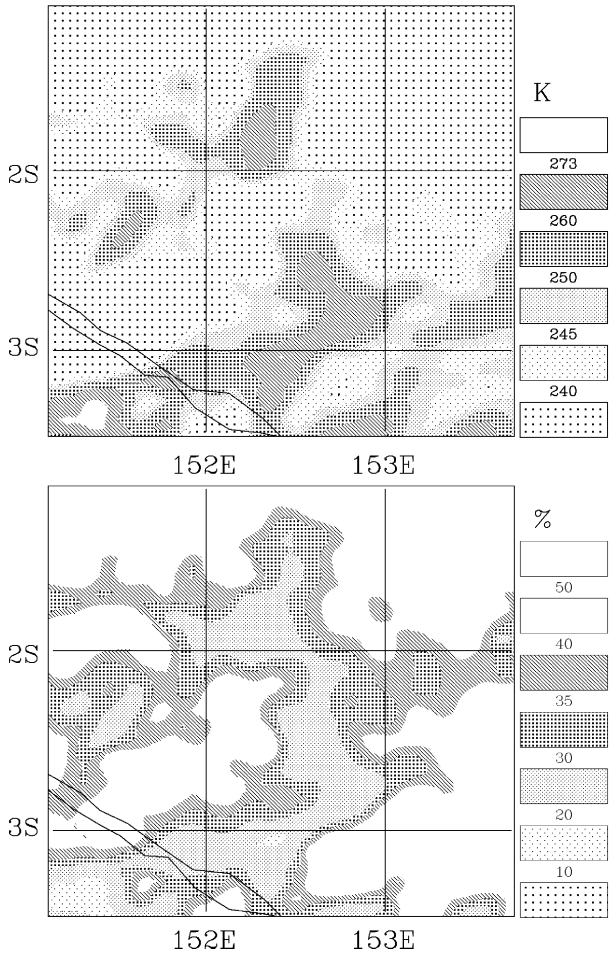

FIG. 11. Shaded areas depict the 0500 UTC 16 Dec 1992 (top) brightness temperature and (bottom) albedo from *NOAA-11* AVHRR satellite. The brightness temperature (albedo) is shown in K (percent).

and Bousquet (1999). However, a careful examination of our results reveals that the lower vorticity maximum was already present in the initial conditions and its presence was maintained by the TE flow during the simulation. The peak value of the major maximum around 550 hPa is about 4.0×10^{-5} s^{-1}, about 4 times weaker than the value of 1.5×10^{-4} s^{-1} found in Chong and Bousquet (1999). This difference can be partly accounted for by the use of a much higher resolution (1 km) dataset by Chong and Bousquet (1999).

To determine whether the vorticity maximum is indeed an MCV, we show in Figs. 14a and 14b the 500-hPa wind vectors and relative vorticity at 0400 and 1600 UTC. The wind vector field represents the total wind because an examination of the instantaneous precipitation plots (not shown) indicated that the MPF is quasi-stationary in the region of the MCV except during the 1 h preceding the 0600 and 1100 UTC convective onsets. In other words, storm-relative winds are the same as earth-relative winds. No closed wind circulation is evident at 0400 UTC. However a closed circulation begins to emerge as the relative vorticity builds up between 0400 and 1600 UTC. This resulting vorticity magnitude therefore fits the definition of an MCV by Zhang (1992). The simulated MCV is approximately 150 km in diameter (see domain V in Fig. 1 and wind circulation in Fig. 14). The location, size, and elevation of the simulated MCV are comparable to the observed.

b. Vertical structure

We present here the vertical kinematic structure of the MCV. Since the MPF is quasi-stationary in the region of the MCV except during the 1 h preceding the 0600 and 1100 UTC convective onsets, the streamlines relative to the storm are the same as streamlines relative to the earth.

It is clear from Fig. 15 that denoting the distance along the line by x, there is an inflow associated with the midlevel MCV in the lowest 1 (2) km between $x =$ 0–180 ($x =$ 240–420) km. Since the average top of the ABL occurs around 500 m, air parcels are rising more than the depth of the ABL, which is consistent with the finding in Kingsmill and Houze (1999).

At 0600 and 1100 UTC, streamlines in the lowest 1–3-km layer for $x =$ 0–180 km exhibit some characteristics of gravity waves with stagnation (Crook and Moncrieff 1988). It is also evident at 1600 UTC, but only occurring in the lowest 1.5 km (Fig. 15c). Dudhia and Moncrieff (1987) also reported such gravity wave–type flow during the entire simulation of an African squall line.

At 0600 UTC, the flow above 3 km for $x =$ 0–180 km is opposite in direction to the flow below 1 km. However, by 1600 UTC, the flow between 3 and 8 km and the low-level flow are in the same direction. An examination of the horizontal streamlines between 3 and 8 km (not shown) indicates that the change in wind direction is the result of a westward migration of the circulation center of the TE flow.

Figure 15 also shows a convectively generated deep ascent into the MPF at 0600 UTC for $x =$ 180–300 km. This ascent is shifted to $x =$ 180–240 km at 1100 and 1600 UTC. Note that the ascending motion at 1100 UTC below 5 km over $x =$ 180–240 km is replaced by descending motion at 1600 UTC (Figs. 15b,c). This results in a cloud-free condition below 1 km over the region (Fig. 15c).

The MCV is characterized with a midlevel high wind speed, ranging between 4 and 8 m s^{-1}, from upstream (i.e., over $x =$ 300–500 km; see Fig. 15a). The midlevel wind is peaked at 1100 and 1600 UTC, with a speed of about 9 m s^{-1} located at an altitude of 6 km at $x =$ 500 km (Figs. 15b,c). A similar vertical structure of the midlevel inflow also appears in the DRY run except for the presence of weaker wind speed (not shown), suggesting that the midlevel inflow is associated with the large-scale upper-level easterly flow. Between $x =$ 240–480 km, Figs. 15b and 15c show that the midlevel inflow

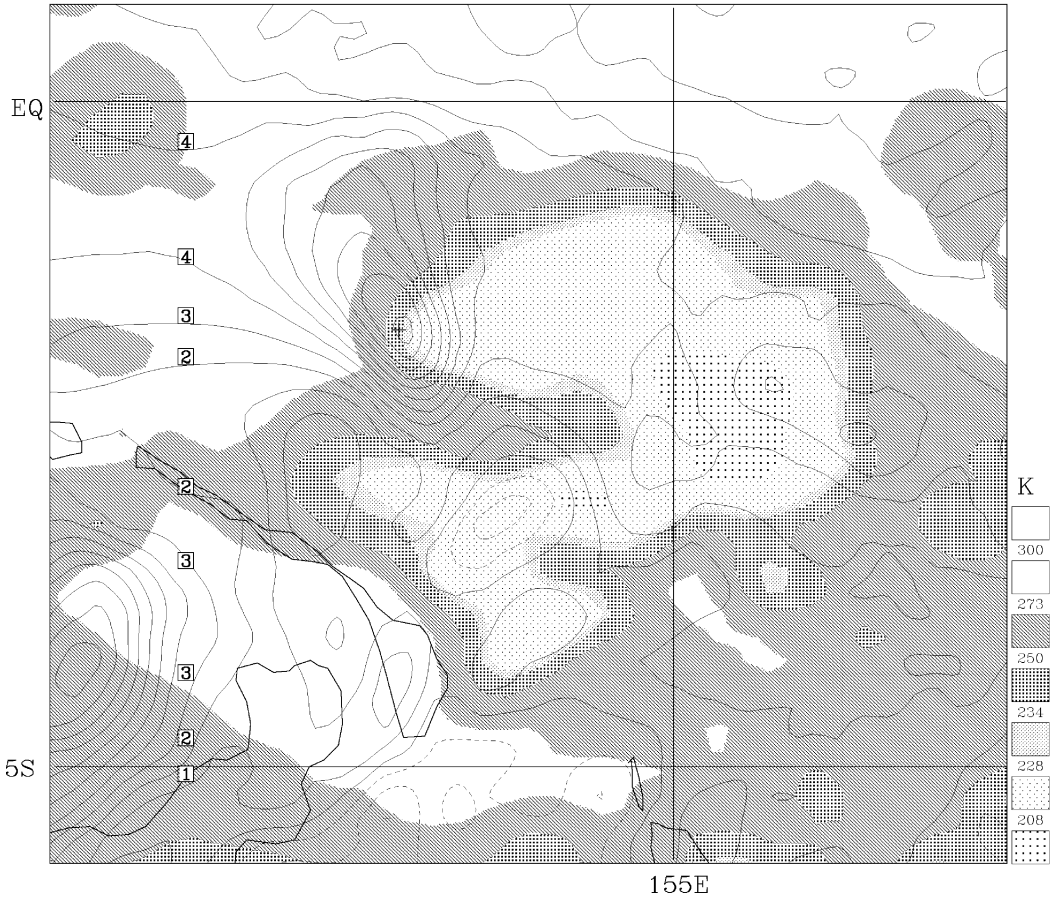

FIG. 12. Shaded areas show the 1130 UTC 15 Dec 1992 brightness temperature (K) from the Japanese GMS satellite along with the 500-hPa simulated relative vorticity at intervals of 1.0×10^{-5} s^{-1} at 1600 UTC.

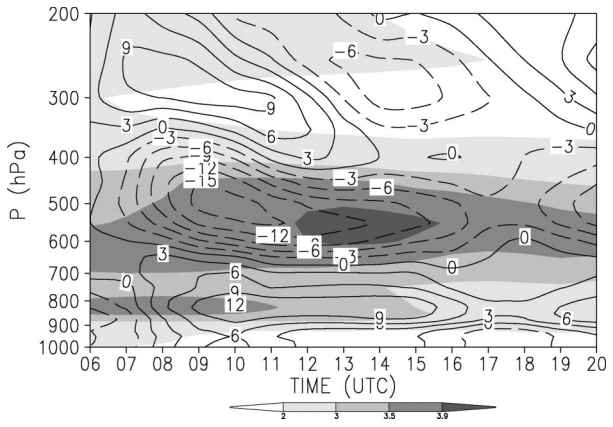

FIG. 13. Time–height cross section of area-averaged relative vorticity (shaded) in units of 10^{-5} s^{-1} and horizontal divergence (contoured) in units of 10^{-6} s^{-1}. The average is calculated over box A, depicted in Fig. 1. Solid (dashed) lines indicate divergence (convergence).

descends to an altitude of 1 km. The descent is driven by the cooling from evaporation of cloud water and rainwater, sublimation, as well as melting of ice particles at the freezing level.

In summary, the MCV circulation is characterized by an inflow layer deeper than the depth of the ABL, a midlevel descending inflow with maximum wind speed 6–8 m s^{-1}. These features are consistent with the conceptual picture proposed by Kingsmill and Houze (1999, their Fig. 20). On the other hand, over $x = 0$–180 km, the low-level inflow shows characteristics of gravity waves with stagnation, whereas the circulation above is governed by the time evolution of the TE flow.

c. Relative vorticity budget

Of interest is that the maximum relative vorticity is confined to the 1–2-km layer at 0600 UTC (Fig. 15a) but shifted to the midlevel afterward (Figs. 15b,c), with an increase in anticyclonic vorticity (positive values indicate anticyclonic vorticity in the Southern Hemisphere) in the 4–7-km layer. Above ($z = 10$–14 km, $x = 0$–120 km) and below ($z = 1$–2 km, $x = 200$–360

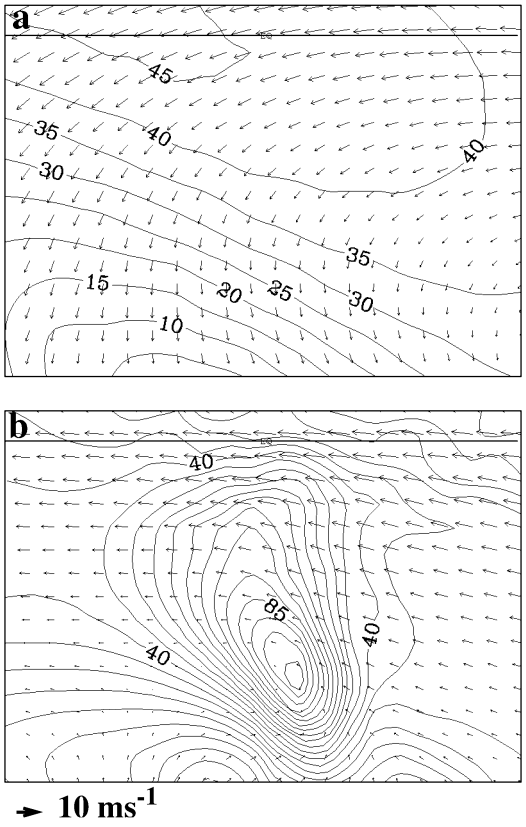

FIG. 14. The 500-hPa wind vector and relative vorticity at intervals of 5×10^{-6} s^{-1} at (a) 0400 and (b) 1600 UTC for experiment CTL.

km) this level, the relative vorticity decreases (Figs. 15a,c).

To examine the physical processes leading to the intensification of the midlevel MCV, the area-averaged vertical vorticity in height coordinates is calculated from

$$\frac{\partial \zeta}{\partial t} = -\mathbf{V}\cdot\nabla\eta - w\frac{\partial \zeta}{\partial z} - (\zeta + f)\nabla\cdot\mathbf{V} + \left(\frac{\partial u}{\partial z}\frac{\partial w}{\partial y} - \frac{\partial v}{\partial z}\frac{\partial w}{\partial x}\right) + \left(\frac{\partial p}{\partial x}\frac{\partial \alpha}{\partial y} - \frac{\partial p}{\partial y}\frac{\partial \alpha}{\partial x}\right) + \frac{\partial}{\partial x}\left(\frac{\partial v_f}{\partial t}\right) - \frac{\partial}{\partial y}\left(\frac{\partial u_f}{\partial t}\right), \quad (1)$$

where η, u_f, and v_f are the vertical component of absolute vorticity and zonal and meridional frictional wind components, respectively, and the other variables assume their conventional meaning. The terms on the right-hand side of (1) represent, respectively, the horizontal advection of absolute vorticity, the vertical advection of relative vorticity, the vortex stretching due to horizontal convergence, the twisting/tilting of horizontal vorticity by nonuniform vertical motion, the solenoidal term, and the frictional generation of vorticity. The last term is expressed following Zhang and Bao (1996). The various terms are computed explicitly during model integration, giving a residual-free budget. At 1100 UTC, the maximum vorticity of the MCV is located in the 4–7-km layer. The vorticity pattern at $z =$ 4.875 km is oriented in a north–south direction with a single maximum lying close to the circulation center of the MCV (Fig. 16a). At 1600 UTC, the pattern tilts northwestward (Fig. 16b) in response to the horizontal advection of absolute vorticity (not shown). To obtain the vorticity budget, we computed the horizontal average of various terms in (1) over box V every time step of the model integration. These terms are then summed and averaged between 0400 and 1600 UTC to yield 12-h time averages.

The local relative vorticity tendency (T. Tend) depicted in Fig. 17 indicates strong intensification of positive vorticity from 3 to 6 km. The increase arises mainly from the stretching term (STR). Vertical advection (VADV) also contributes positively from 3 to 5 km but is counteracted somewhat by negative horizontal advection (HADV). The contributions from the tilting (TILTING) and solenoidal (SOLEN) terms are small but positive. Past studies highlighted the role of tilting in initiating the development of the MCV (e.g., Davies and Weisman 1994). This tilting effect is relatively small because of the absence of strong vertical shear. By comparison, there was a moderate concentration of midlevel vertical vorticity at the model initial time, which is associated with the transequatorial flow (partly shown in Fig. 14a); this midlevel circulation center is shifted to the southeast compared to its center at 900 hPa (Fig. 2a). Thus, it is the transequatorial circulation that provides an initial positive vertical vorticity for the development of the MCV through vortex stretching.

The local time rate of change of vorticity becomes negative from 6 to 10 km, and is contributed by the tilting, solenoidal, and stretching terms in that order. On the other hand, horizontal advection and vertical advection are the positive contributors. However, for the layers above (i.e., 10 to 15 km), horizontal advection becomes strongly negative to cause a negative vorticity tendency, although the solenoidal, vertical advection, and tilting contributions are positive.

Between 1 and 3 km, relative vorticity also decreases with time, mainly as a result of the tilting, stretching, and the solenoidal effects. Vertical advection contributes positively above 1.5 km. The frictional destruction of relative vorticity (FRIC) is small except in the lowest 500 m and near the level of the tropopause.

Thus, the midlevel MCV is generated and intensified largely by vortex stretching. This is similar to the findings of Johnson and Bartels (1992) and Rogers and Fritsch (2001) for mesovortices associated with midlatitude MCSs. They found that the production of vorticity was dominated by vortex stretching, with relatively minor contribution from tilting, again due to the MCV development in weak-gradient environments. The

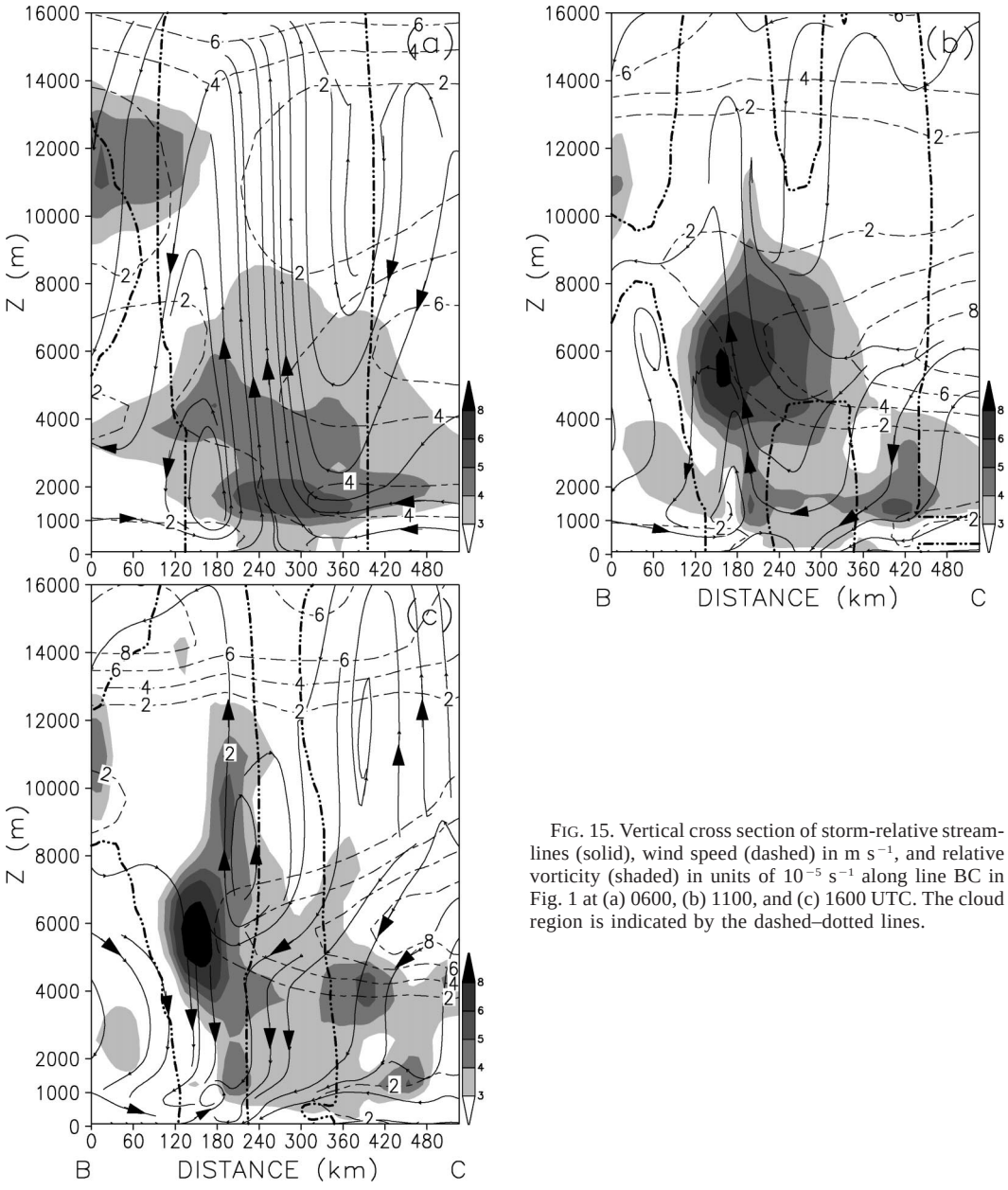

FIG. 15. Vertical cross section of storm-relative streamlines (solid), wind speed (dashed) in m s^{-1}, and relative vorticity (shaded) in units of 10^{-5} s^{-1} along line BC in Fig. 1 at (a) 0600, (b) 1100, and (c) 1600 UTC. The cloud region is indicated by the dashed–dotted lines.

vertical divergence profile averaged over box V (Fig. 18) shows midlevel convergence around $z = 6$ km height with ascent above and descent below. In our simulation, the Kain–Fritsch convective parameterization was used, and the peak convective heating occurs around 550 hPa (or 6 km). Hence, the initiation and maintenance of the MCV in our case is largely driven by the upper-level heating associated with persistent deep convection. Similar to our findings, Kain and Fritsch (1990) also reported an elevated heating peak associated with deep convection for an Australian Monsoon Experiment (AMEX) sounding. Keenan and Rutledge (1993) found that a warm-core MCV was maintained by thermodynamically induced convergence in the midtroposphere. Thus, the MCV in the vicinity of the 0600 convective onset shares many characteristics of mesovortices reported from the Tropics and midlatitudes. The mesovortex constitutes an important organized feature of the 15 December 1992 TOGA COARE MCS.

Recall that the present MCS developed because of four convective onsets (Fig. 1). Although the MCV occurred in the vicinity of the first onset, the subsequent convective onsets were largely controlled by the evolution of the vertical motion associated with the TE circulation and the westward propagation of the quasi-2-day wave. This suggests that the MCV plays little role in the subsequent initiation of the MPFs that formed the MCS.

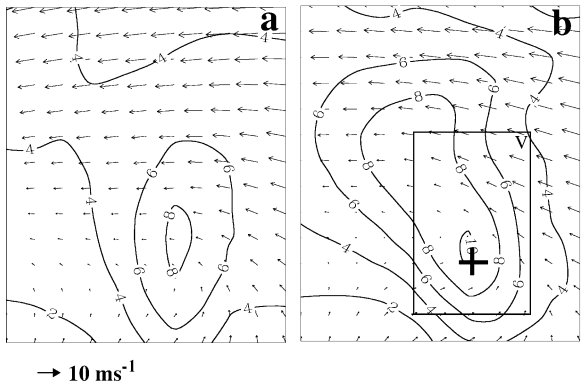

FIG. 16. Vertical relative vorticity in units of 10^{-5} s^{-1} and horizontal wind vectors at an altitude of 4.875 km at (a) 1100 and (b) 1600 UTC. The symbol "+" shows the circulation center associated with the MCV in box V, which is also indicated in Fig. 1.

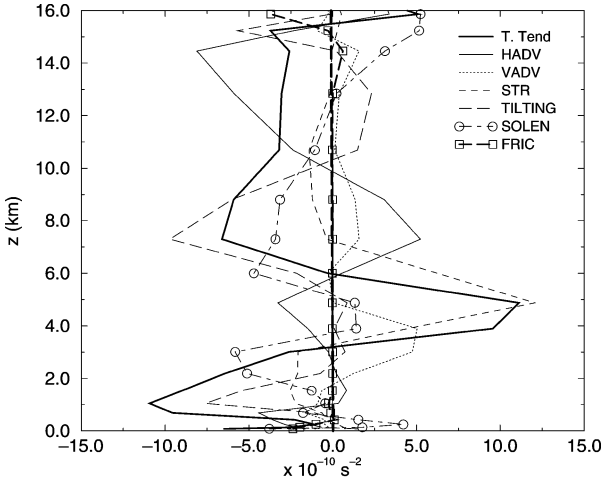

FIG. 17. Vertical profiles of the terms in the vorticity budget equation (1). The profiles denote 12-h time averages between 0400 and 1600 UTC and are also averaged horizontally over box V in Fig. 16b.

d. Warm-core MCV

Two types of mesovortices, the heating-induced warm core and a cooling-induced vortex, have been observed in the stratiform regions of MCSs. The former is peaked beneath the major ascending portion while the latter beneath the descending portion of MCSs. The warm-core circulation develops in the presence of little vertical shear as buoyant air rises and induces convergence to amplify the vertical vorticity at midlevels (Zhang et al. 1988). The cooling-induced vortex is associated with the descending rear inflow that intensifies the vorticity through tilting in the presence of strong vertical shear and stretching by midlevel convergence (Zhang 1992).

To determine whether the simulated mesovortex is warm-cored, we calculated the temperature perturbation relative to the environment. However, the signal was too weak to allow a definitive judgement. The weak temperature perturbation arises because of the large local Rossby radius, because the MCV is situated close to the equator. In order for the latent heat release associated with moist convection to result in a warm perturbation in the midtroposphere, the local Rossby radius must be reduced to a scale comparable to the horizontal scale of heating (Rogers and Fritsch 2001). The reduction in the Rossby radius can come about by preexisting vorticity and/or diabatic heating due to sustained convection. Nevertheless, because the present MCV develops in the ascending branch of the MCS as a result of vortex stretching in the midtroposphere and because the vertical wind shear is extremely weak (LeMone et al. 1998), the simulated MCV shares characteristics that are consistent with those found in a warm-core MCV.

e. Large-scale circulation and MCV

Rogers and Fritsch (2001) studied the development of a midlatitude surface cyclone due to the convectively generated MCVs. They suggested a cooperative interaction between an MCV and moist convection. Deep convection was forced by external environmental factors (e.g., favorable positioning of an upper-level trough) and if sustained for a sufficient period of time, the vertical column may become saturated. The diabatic heating within this saturated environment helps in the development of a midlevel MCV through stretching the preexisting vertical vorticity. Similar findings were also suggested by Zhang and Fritsch (1987) in their study of a warm-core MCV that occurred in a midlatitude MCC. Thus, regions characterized by large-scale ascent for a sufficient period of time are the favorable areas of

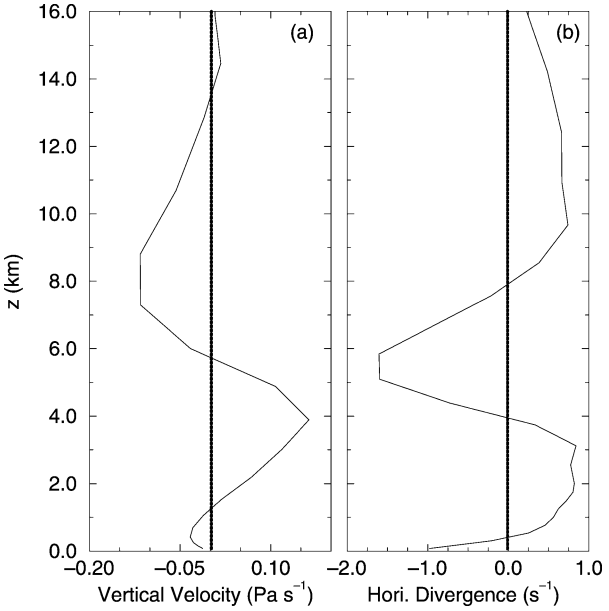

FIG. 18. Vertical profiles of (a) vertical velocity (Pa s^{-1}) and (b) horizontal divergence (s^{-1}). The profiles denote 12-h time averages between 0400 and 1600 UTC and are also averaged horizontally over box V in Fig. 16b.

MCV formation, provided that the midlevels are characterized by the existence of vertical vorticity (e.g., associated with a pressure trough).

As mentioned before, the large-scale upward motion is one of the factors causing the convective onset. Thus, if the upward motion is sustained for a long period of time after the convective onset, it could lead to the formation of an MCV. We noted that the third and fourth convective onsets (Fig. 1) are regulated by the temporal evolution of the westward-propagating quasi-2-day wave. The vertical velocity structure (upward in association with tilted zonal wind structures; Fig. 6) propagates westward sustaining upward motion for about 3–4 h over a distance of about 150 km (approximate dimension of the simulated MCV). This suggests that although the wave-induced upward motion is responsible for the convective onset, it is less favorable for persistent deep convection. Therefore, no MCV develops in the region of the third and fourth convective onset.

In the case of the second convective onset that forms in a region of confluence south of the center of the TE flow (Fig. 2d), the migration of the TE flow between 0800 and 1700 UTC (Figs. 2b,d and 4b,d) results in an absence of the confluence zone after 0800 UTC. This precludes the formation of an MCV. On the other hand, in the region of the first convective onset located southwest of the center of the TE circulation, there is confluence between 0400 and 1700 UTC (Figs. 2b,d and 4b,d). At 0400 UTC, the TE flow occurs with its circulation center at 500 hPa shifted to the southeast compared to its center at 900 hPa (Figs. 14a and 2a). Thus the transequatorial circulation extends all the way up to the midlevels and provides anticyclonic environmental vorticity. Therefore, in the presence of sustained upward motion and midlevel vertical vorticity, the first onset region is conductive to the development of the MCV. Chong and Bousquet (1999) reported the occurrence of an MCV in the 13 December 1992 TOGA COARE MCS, which was located southwest of a large-scale TE circulation centered around 165°E. This suggests that an MCS occurring near the TE circulation over the warm pool is likely to be associated with an MCV.

4. Summary and conclusions

In this study, a 16-h (i.e., 0400–2000 UTC 15 December 1992) numerical simulation of the life cycle of a class 4 TOGA COARE MCS is used to study the processes that are responsible for the convective onsets during its growing and mature stages and for the development of a midlevel mesovortex near the location of the first convective onset.

During the *growing stage* of the MCS (0400–1700 UTC), the simulation results suggested that three MPFs were initiated at 0600, 1100, and 1400 UTC. During the *mature stage,* the MCS exhibited two MPFs characterized by two NE–SW-oriented convective lines (L_1 and L_2) with stratiform precipitation located to the northwest. We address the convective onsets in terms of surface potential temperature drop-off (SPTD), the presence of large-scale ascent, and CAPE.

The 0600 UTC convective onset occurs as a result of the existence of large-scale ascent, CAPE, and favorable SPTD in the model initial conditions (0400 UTC). The 1100 UTC convective onset is regulated by the favorable occurrence of SPTD between 0400 and 0800 UTC. Specifically, an increase in SPTD is caused by a decrease in the ABL potential temperature. The decrease is effected by longwave cooling, and the vertical cold advection of potential temperature is associated with large-scale ascent in the confluence zone. As shown in NYZ01, the specification of the SPTD threshold was important in obtaining the successful simulation of the life cycle of the 15 December 1992 MCS. The 1400 and 1700 UTC convective onsets are regulated by the development of upward motion associated with the westward propagation of the quasi-2-day wave. The four MPFs initiated at different locations clustered together to form the MCS. The gravity wave mechanism suggested by Mapes (1993) does not play a role in the initiation of the MPFs. Instead, the evolution of the vertical motion is responsible for their initiation. Although the present study is confined to one case, it is likely that the 2-day wave played a role in other cases. Specifically, Takayabu et al. (1996) suggested the existence of eight quasi-2-day wave events from 10 to 16 and 21 to 27 December 1992 (their Fig. 4). Thus, it is possible that the vertical motion associated with the eight wave events regulated the December 1992 TOGA COARE convective events over the warm pool. If so, the existence of the 2-day wave and the transequatorial (TE) circulation in the near-equatorial latitudes may result in an enhanced predictability of the MCS.

Our diagnosis of the simulated relative vorticity field suggested the presence of a mesovortex in the vicinity of the first convective onset, which is consistent with satellite observations. Its vertical circulation is characterized by an inflow layer deeper than the ABL depth, a midlevel inflow with the maximum wind speed confined to the 4–8-km layer, and the descent of the midlevel flow to the 1-km level, as noted by Kingsmill and Houze (1999, their Fig. 20). The inflow in the 1–3-km layer resembles a gravity wave with stagnation, while the 3–8-km flow is governed by the time evolution of the TE flow.

The midlevel MCV is generated and intensified largely by vertical advection of vorticity and vortex stretching. A horizontally averaged divergence profile shows peak convergence around 6-km height caused by upper-level heating associated with persistent deep convection. At midlevels, there is a negative correlation between horizontal advection and stretching, suggesting the role of advection in redistribution of vorticity reported by Brandes and Ziegler (1993), Verlinde and Cotton (1990), and Chong and Bousquet (1999). Although the temperature perturbation associated with the MCV is

too weak to definitively categorize the MCV as warm-core, our results suggest that the MCV shares characteristics that are found in warm-core MCVs.

Above the MCV, the reduction of the relative vorticity arises because of the combined effects of tilting and horizontal advection. Below the MCV, contributions to the reduction in relative vorticity arise from tilting, stretching, and the solenoidal term. The mean vertical motion is upward (downward) above (below) the MCV and is effective in yielding positive vertical advection of relative vorticity throughout much of the troposphere.

While MCVs associated with midlatitude MCSs have been extensively studied, this paper represents the second study characterizing a near-equatorial MCV. Although the MCV shares several features associated with other low and midlatitude MCSs, our results suggest that the MCV played little role in the initiation of the second, third, and fourth convective onsets. This is in contrast to the findings of Zhang and Fritsch (1987), who found that the MCV circulation impacted the subsequent development of convection. In our case, it is the large-scale TE flow region that provides a favorable environment for the MCV development. With the occurrence of such near-equatorial MCVs reported for another TOGA COARE MCS by Chong and Bousquet (1999), MCVs are likely to be associated with other large warm-pool MCS occurring in the vicinity of the TE flow.

Acknowledgments. We wish to thank Dr. Yubao Liu for generating the initial conditions using the Pennsylvania State University–National Center for Atmospheric Research (PSU–NCAR) MM5 preprocessor system. We thank the TOGA COARE International Project Office (TCIPO) for providing us with the GMS satellite imagery data. We wish to thank Dr. Yongsheng Chen for his help with the figures. This research was supported by the Meteorological Service and the Natural Science and Engineering Research Council of Canada. The third author, DLZ, was supported by the NSF Grant ATM-9802391, NASA Grant NAG-57842, and ONR Grant N00014-96-1-0746. The constructive suggestions of two anonymous reviewers significantly improved the presentation of the results.

REFERENCES

Bartels, D. L., and R. A. Maddox, 1991: Midlevel cyclonic vortices generated by mesoscale convective systems. *Mon. Wea. Rev.*, **119,** 104–188.

Benoit, R., J. Cote, and J. Mailhot, 1989: Inclusion of a TKE boundary layer parameterization in the Canadian regional finite-element model. *Mon. Wea. Rev.*, **117,** 1726–1750.

——, M. Desgagne, P. Pellerin, S. Pellerin, Y. Chartier, and S. Desjardins, 1997: The Canadian MC2: A semi-Lagrangian, semi-implicit wideband atmospheric model suited for finescale process studies and simulation. *Mon. Wea. Rev.*, **125,** 2382–2415.

Betts, A. K., 1986: A new convective adjustment scheme. Part I: Observational and theoretical basis. *Quart. J. Roy. Meteor. Soc.*, **112,** 667–691.

Brandes, E. A., and C. L. Ziegler, 1993: Mesoscale downdraft influences on vertical vorticity in a mature mesoscale convective system. *Mon. Wea. Rev.*, **121,** 1337–1353.

Chen, S. S., and R. A. Houze, 1996: Multiscale variability of deep convection in relation to large-scale circulation in TOGA COARE. *J. Atmos. Sci.*, **53,** 1380–1409.

——, and ——, 1997: Diurnal variation and life-cycle of deep convective systems over the tropical Pacific warm pool. *Quart. J. Roy. Meteor. Soc.*, **123,** 357–388.

Chong, M., and O. Bousquet, 1999: A mesovortex within a near-equatorial mesoscale convective system during TOGA COARE. *Mon. Wea. Rev.*, **127,** 1145–1156.

Crook, N. A., 1996: Sensitivity of moist convection forced by boundary layer processes to low-level thermodynamic fields. *Mon. Wea. Rev.*, **124,** 1767–1785.

——, and M. W. Moncrieff, 1988: The effect of large-scale convergence on the generation and maintenance of deep moist convection. *J. Atmos. Sci.*, **45,** 3606–3624.

Davies, C. A., and M. L. Weisman, 1994: Balanced dynamics of mesoscale vortices produced in simulated convective systems. *J. Atmos. Sci.*, **51,** 2005–2030.

Dudhia, J., and M. W. Moncrieff, 1987: A numerical simulation of quasi-stationary tropical convective bands. *Quart. J. Roy. Meteor. Soc.*, **113,** 926–967.

Errico, R. M., 1985: Spectra computed from a limited area grid. *Mon. Wea. Rev.*, **113,** 1554–1562.

Fairall, C. W., E. F. Bradley, D. P. Rogers, J. B. Edson, and G. S. Young, 1996: Bulk parameterization of air–sea fluxes for Tropical Ocean-Global Atmosphere Coupled-Ocean Atmosphere Response Experiment. *J. Geophys. Res.*, **101,** 3747–3764.

Garand, L., and J. Mailhot, 1990: The influence of infrared radiation on numerical weather forecasts. *Proc. Seventh Conf. on Atmospheric Radiation,* San Francisco, CA, Amer. Meteor. Soc., J146–J151.

Jabouille, P., J. L. Redelsperger, and J. P. Lafore, 1996: Modification of surface fluxes by atmospheric convection in the TOGA COARE region. *Mon. Wea. Rev.*, **124,** 816–837.

Johnson, R. H., and D. L. Bartels, 1992: Circulations associated with a mature-to-decaying midlatitude mesoscale convective system. *Mon. Wea. Rev.*, **120,** 1301–1320.

Johnston, E. C., 1981: Mesoscale vorticity centers induced by mesoscale convective complexes. M.S. thesis, Dept. of Meteorology, University of Wisconsin—Madison, 54 pp.

Kain, J. S., and J. M. Fritsch, 1990: A one-dimensional entraining/detraining plume model and its application in convective parameterization. *J. Atmos. Sci.*, **47,** 2784–2802.

Keenan, T. D., and S. A. Rutledge, 1993: Mesoscale characteristics of monsoonal convection and associated stratiform precipitation. *Mon. Wea. Rev.*, **121,** 352–374.

Kingsmill, D. E., and R. A. Houze, 1999: Kinematic characteristics of air flowing into and out of precipitating convection over the west Pacific warm pool: An airborne Doppler radar survey. *Quart. J. Roy. Meteor. Soc.*, **125,** 1165–1207.

Kong, F. Y., and M. K. Yau, 1997: An explicit approach to microphysics in MC2. *Atmos.–Ocean,* **35,** 257–291.

Leary, C. A., and R. A. Houze, 1979: The structure and evolution of convection in a tropical cloud cluster. *J. Atmos. Sci.*, **36,** 437–457.

LeMone, M. A., E. J. Zipser, and S. B. Trier, 1998: The role of environmental shear and thermodynamic conditions in determining the structure and evolution of mesoscale convective systems during TOGA COARE. *J. Atmos. Sci.*, **55,** 3493–3518.

Mapes, B. E., 1993: Gregarious tropical convection. *J. Atmos. Sci.*, **50,** 2026–2037.

——, and R. A. Houze, 1993: Cloud clusters and superclusters over the oceanic warm pool. *Mon. Wea. Rev.*, **121,** 1398–1415.

Miller, M., and J. M. Fritsch, 1991: Mesoscale convective complexes in the western Pacific region. *Mon. Wea. Rev.*, **119,** 2978–2992.

Nagarajan, B., M. K. Yau, and D.-L. Zhang, 2001: A numerical study of a mesoscale convective system during TOGA COARE. Part

I: Model description and verification. *Mon. Wea. Rev.,* **129,** 2501–2520.

Numaguti, A., 1995: Characteristics of 4-to-20-day period disturbances observed in the equatorial Pacific during the TOGA COARE IOP. *J. Meteor. Soc. Japan,* **73,** 353–377.

Protat, A., and Y. Lemaitre, 2001a: Scale interactions involved in the initiation, structure, and evolution of the 15 December 1992 MCS observed during TOGA COARE. Part I: Synoptic-scale processes. *Mon. Wea. Rev.,* **129,** 1757–1778.

——, and ——, 2001b: Scale interactions involved in the initiation, structure, and evolution of the 15 December 1992 MCS observed during TOGA COARE. Part II: Mesoscale and convective-scale processes. *Mon. Wea. Rev.,* **129,** 1779–1808.

Ramage, C. S., 1971: *Monsoon Meterology*. Vol. 15, Academic Press, 296 pp.

Raymond, D. J., 1995: Regulation of moist convection over the west Pacific warm pool. *J. Atmos. Sci.,* **52,** 3945–3959.

Rickenbach, T. M., and S. A. Rutledge, 1998: Convection in TOGA COARE: Horizontal scale, morphology, and rainfall production. *J. Atmos. Sci.,* **55,** 2715–2729.

Rogers, R. F., and J. M. Fritsch, 2001: Surface cyclogenesis from convectively driven amplification of midlevel mesoscale convective vortices. *Mon. Wea. Rev.,* **129,** 605–637.

Takayabu, Y. N., K.-M. Lau, and C.-H. Sui, 1996: Observation of a quasi-2-day wave during TOGA COARE. *Mon. Wea. Rev.,* **124,** 1892–1913.

Tollerud, E. I., and S. K. Esbensen, 1985: A composite life cycle of nonsquall mesoscale convective systems over the tropical ocean. Part I: Kinematic fields. *J. Atmos. Sci.,* **42,** 823–837.

Verlinde, J., and W. R. Cotton, 1990: A mesovortex couplet observed in the trailing anvil of a multicellular convective complex. *Mon. Wea. Rev.,* **118,** 993–1010.

Webster, P. J., and R. Lukas, 1992: TOGA COARE: The Coupled Ocean Atmosphere Response Experiment. *Bull. Amer. Meteor. Soc.,* **73,** 1377–1416.

——, C. A. Clayson, and J. A. Currie, 1996: Clouds, radiation, and the diurnal cycle of sea surface temperature in the tropical western Pacific. *J. Climate,* **9,** 1712–1730.

Yuter, S. E., R. A. Houze, F. Smull, F. D. Marks, J. R. Daugherty, and S. R. Brodzik, 1995: TOGA COARE aircraft mission summary images: An electronic atlas. *Bull. Amer. Meteor. Soc.,* **76,** 319–328.

Zhang, D.-L., 1992: The formation of a cooling-induced mesovortex in the trailing stratiform region of a midlatitude squall line. *Mon. Wea. Rev.,* **120,** 2763–2785.

——, and J. M. Fritsch, 1987: Numerical simulation of the meso-β-scale structure and evolution of the 1977 Johnstown flood. Part II: Inertially stable warm-core vortex. *J. Atmos. Sci.,* **44,** 2593–2612.

——, and N. Bao, 1996: Ocean cyclogenesis as induced by a mesoscale convective system moving offshore. Part I: A 90-h real-data simulation. *Mon. Wea. Rev.,* **124,** 1449–1469.

——, E.-Y. Hsie, and M. W. Moncrieff, 1988: A comparison of explicit and implicit predictions of convective and stratiform precipitating weather systems with a meso-β-scale numerical model. *Quart. J. Roy. Meteor. Soc.,* **114,** 31–60.